Theoretical Electron Mobility Analysis in Thin-Body FETs: Dependence on Substrate Orientation and Biaxial Strain

Viktor Sverdlov, Stephan Enzo Ungersboeck, and Hans Kosina, *Member, IEEE*

***Abstract*—Results of recent mobility measurements in ultra-thin-body FETs are analyzed theoretically for different substrate orientations. A Monte Carlo method incorporating the degenerate statistics exactly is used for calculations of the mobility. Due to volume inversion, the mobility in double-gate ultrathin-body (110) FETs is enhanced in comparison with the mobility of single-gate structures, in the whole range carrier concentrations. In contrast, the mobility in a double-gate (100) 3 nm thick structure plotted as a function of the carrier concentration per channel sinks below the single-gate mobility value for high effective fields. It is shown that degeneracy effects play a crucial role in mobility degradation for (100) double-gate FETs, as they lead to the opening of additional intersubband scattering channels. Biaxial strain has little influence on the mobility of ultrathin-body FETs. Simulation results are in good agreement with recent mobility measurements.**

***Index Terms*—Double-gate MOSFET, mobility, Monte Carlo simulations, volume inversion.**

I. Introduction

DOUBLE-GATE (DG) silicon-on-insulator (SOI) transistors with ultrathin Si body (UTB) are considered good candidates for the far-end ITRS roadmap scaling [1]. Excellent electrostatic channel control in DG operation is theoretically predicted allowing scaling of the MOSFET's channel length down to 2.5 nm [2], maintaining reasonable subthreshold slope, satisfactory DIBL, and acceptable gain.

Comparative theoretical analysis of electron mobility behavior in single-gate (SG) and DG FETs is exclusively limited to (100) SOI orientation [3], [4]. Due to an existing discrepancy between the mobility measurements and theoretical predictions for (100) and (110) UTB SOI FETs, theoretical analysis is highly desirable for (110) substrate orientation.

According to the volume inversion concept [5], the inversion layers located at the opposite interfaces of a thick DG structure start intersecting when the Si body thickness shrinks. A charge maximum is formed in the middle of the UTB DG structure, yielding a larger distance between carriers and Si-SiO_2 interfaces. This should eventually result in a substantial decrease of surface roughness scattering in UTB DG structures. Therefore, higher mobility is expected in DG structures compared to their SG analogs for similar body thicknesses. Mobility behavior consistent with this concept was recently reported experimentally for (110) UTB FETs [6]. The electron mobility in UTB DG structures plotted as function of one-half of the total concentration is higher than the SG mobility in the whole range of concentrations. However, the electron mobility in (100) UTB DG structures is found to be smaller than the SG mobility at high effective fields [6], [7], although an enhancement due to bulk inversion would be expected [5].

In this work we study the mobility behavior in SG and DG UTB FETs for substrate orientation (100) and (110). A Monte Carlo algorithm is used which incorporates degeneracy effects *exactly* in the limit of vanishing driving fields and is valid for arbitrary scattering mechanisms and for general band structure [8]. Due to a higher carrier concentration, degeneracy effects are more pronounced in DG structures than in SG structures at similar gate voltages. We demonstrate that the higher Fermi level leads to a substantial increase of intersubband scattering in (100) UTB DG FETs. Higher scattering rates compensate the mobility enhancement due to volume inversion. Biaxial stress is introduced to validate the physical mechanism limiting the low-field mobility in (100) DG structures.

II. Simulation Method

We generalize the Monte Carlo algorithm designed for small signal analysis of the 3-D electron gas [8] to quasi 2-D electron systems. The method is based on the solution of the linearized Boltzmann equation and is formally exact for small driving fields. The method is valid for arbitrary scattering mechanisms and band structure, including multivalley and multisubband cases. In the method the diffusion tensor $D_{\alpha\beta}$ is calculated as an integral of the velocity autocorrelation function [9]

$$D_{\alpha\beta} = \int_0^\infty d\tau \, \langle v_\alpha(t) v_\beta(t+\tau) \rangle \qquad (1)$$

where angular brackets denote the time averaging over stochastic dynamics determined by the rates $\Lambda_{mn}(\mathbf{k},\mathbf{k}')$ of the *linearized* multisubband Boltzmann scattering integral in case of degenerate statistics. The rates $\Lambda_{mn}(\mathbf{k},\mathbf{k}')$ are related to the rates $S_{mn}(\mathbf{k},\mathbf{k}')$ of the original Boltzmann equation as

$$\Lambda_{mn}(\mathbf{k},\mathbf{k}') = (1 - f(E_m(\mathbf{k}')))\, S_{mn}(\mathbf{k},\mathbf{k}') + f(E_m(\mathbf{k}')) S_{mn}(\mathbf{k}',\mathbf{k}), \qquad (2)$$

where $f(E)$ is the Fermi–Dirac distribution function $E_n(\mathbf{k})$ in the total energy in the n-th 2-D subband. The mobility tensor

Manuscript received June 2, 2006; revised December 15, 2006. This work was supported in part by the Austrian Science Fund FWF under Project P17285-N02 and in part by the European Commission under Project SINANO IST-506844. The review of this paper was arranged by Associate Editor D. Frank.

The authors are with the Institute for Microelectronics, Technical University Vienna, A-1040 Vienna, Austria (e-mail: sverdlov@iue.tuwien.ac.at; ungersboeck@iue.tuwien.ac.at; kosina@iue.tuwien.ac.at).

Digital Object Identifier 10.1109/TNANO.2007.894835

1536-125X/$25.00 © 2007 IEEE

$\tilde{\mu}_{\alpha\beta}$ is related to the diffusion tensor via the Einstein relation for degenerate statistics

$$\tilde{\mu}_{\alpha\beta} = eD_{\alpha\beta}\frac{1}{n_0}\frac{dn_0}{dE_F} \tag{3}$$

where e is the electron charge, n_0 is the carrier concentration, and E_F is the Fermi level.

In order to compute the mobility, we accumulate three temporary estimators t, w_β, and $\nu_{\alpha\beta}$ during the Monte Carlo simulations. We summarize the method as follows.

i) Initialize $t = 0$, $w_\beta = 0$, $\nu_{\alpha\beta} = 0$, and start the particle trajectory with the stochastic 0dynamics determined by the scattering rates $\Lambda_{mn}(\mathbf{k}, \mathbf{k}')$ from (2) of the *linearized* multisubband Boltzmann equations.

ii) Before each scattering event update $\nu_{\alpha\beta}$, w_β, and t:

$$\begin{aligned} t &= t + \frac{\tau(j)}{1 - f(E(j))}, \\ w_\beta &= w_\beta + v_\beta(j)\tau(j), \\ \nu_{\alpha\beta} &= \nu_{\alpha\beta} + \tau(j)v_\alpha(j)w_\beta(j). \end{aligned}$$

iii) When t is sufficiently large, compute the mobility tensor as

$$\tilde{\mu}_{\alpha\beta} = \frac{e}{k_B T}\frac{\nu_{\alpha\beta}}{t},$$

where $v_\alpha(j)$ denotes the α-component of the velocity, $E(j)$ is the particle energy, $f(E)$ is the Fermi–Dirac function, and $\tau(j)$ is the time of j-th free flight. The convergence of the method is improved by resetting $w_\beta = 0$ each time a velocity randomizing scattering event occurs.

III. SG and DG Mobilities for (100) and (110) UTB Orientations

The subband energies and corresponding wave functions are calculated from the Schrödinger equation coupled self-consistently with the Poisson equation, for each value of the effective field. For (110) surface orientation, the equation for the envelope functions in quantization direction contains the first-order derivative of the wave functions as well. This derivative can be eliminated from the equation by a unitary wave function transformation [10], which leads to a standard Schrödinger-like equation for the envelope function, allowing the determination of quantization mass, conductivity masses and density-of-state effective mass. For (110) orientation the subband structure consists of a fourfold degenerate, unprimed, and a twofold degenerate, primed subband ladder. Subbands in both ladders are highly anisotropic. The wave functions are then used to calculate the scattering rates. Our transport calculations account for electron–phonon interactions [11], [12] and surface roughness scattering, which are the dominant mechanisms determining the mobility in the region of high effective fields. We use the original formulation by Prange and Nee [13]–[15] for the surface roughness scattering matrix elements

$$|M_{ij}(q)|^2 = \left[\frac{\hbar^2}{2m_z}\psi_i'(z_0)\psi_j'(z_0)\right]^2 \frac{S_{SR}(q)}{\varepsilon_{ij}^2(q)} \tag{4}$$

TABLE I
Surface Roughness Correlation Function Parameters and Acoustic Deformation Potential D_{ADP} Used For (100) and (110) UTB Orientations

	(100)	(110)
Λ	1.5 nm	1.5 nm
Δ	0.47 nm	0.6 nm
D_{ADP}	14 eV	13 eV

where m_z is the quantization mass, $\psi_i'(z_0)$ is the derivative of the i-th subband wave function $\psi_i(z)$ at the interface $z = z_0$, and $S_{SR}(q)$ is the surface roughness correlation function. The surface roughness is assumed to be uncorrelated and equal at the two interfaces of a UTB structure. We adopt the surface roughness correlation function $S_{SR}(q)$ to be of a Gaussian shape

$$S_{SR}(q) = \pi\Delta^2\Lambda^2 \exp\left(-\left(\frac{q\Lambda}{2}\right)^2\right) \tag{5}$$

where Δ and Λ are two parameters corresponding to characteristic roughness amplitude and correlation length. The choice of the correlation function in a Gaussian form is not critical for the conclusions of this work and is adopted for convenience. Static dielectric screening is taken into account, following the model [16]–[18]

$$\varepsilon_{ij}(q) = \begin{cases} 1 + \frac{e^2}{2\varepsilon_{SC} q}\sum_n F_n(q)\Pi_n(q), & i = j \\ 1, & i \neq j \end{cases} \tag{6}$$

where $\varepsilon_{\mathrm{SC}}$ is the Si lattice dielectric constant, $\Pi_n(q)$ is the polarization factor in the n-th subband ([17, Eq. (14)]), and $F_n(q)$ is the formfactor

$$F_n(q) = \int_0^{t_{\mathrm{SI}}}\int_0^{t_{\mathrm{SI}}} dz dz' \psi_n^2(z) G(z, z'; q)\psi_n^2(z').$$

The Green's function $G(z, z'; q)$ is determined by [14, Eq. (32)]. The scattering model captures the main difference of the mobility characteristics in DG and SG structures at high concentrations for different orientations, as we demonstrate below.

In this work, the nonparabolicity effects are taken into account by choosing a nonparabolicity parameter $\alpha = 0.5\mathrm{eV}^{-1}$ [19]. The parameters of the surface roughness correlation function and the acoustic deformation potential are calibrated in order to reproduce the experimental mobility in thick (100) SG FETs [20]. The parameters are summarized in Table I. We use the same parameters to calculate mobilities for smaller body thicknesses, both for DG and SG FETs.

Due to the anisotropy of the subbands, the surface mobility at (110) interface is also anisotropic. We have calibrated the surface roughness parameters and the acoustic deformation potential in order to reproduce the experimental mobility along $\langle 001\rangle$ and $\langle 1\bar{1}0\rangle$ directions [6]. The parameters are summarized in Table I.

In thick Si body DG FETs the inversion channels located at the opposite interfaces can be considered independent. Due to the separation of the inversion layers, the mobility measured as a function of carrier concentration per *single* channel $N_{\mathrm{DG}}/2$ must coincide with the mobility in thick SG structures [6] plotted as a function of SG inversion concentration N_{SG}. The DG mobility calculated for a 20 nm thick body is indeed in

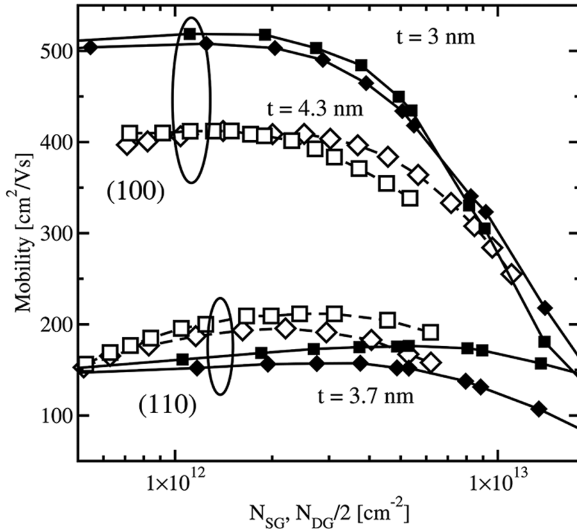

Fig. 1. Low field mobility simulations for (100) and (110) oriented UTB FETs. Open symbols stand for experimental data from [7] for (100) 4.3 nm UTB FETs and from [6] for (110) 3.7 nm UTB FETs. Closed symbols are simulation results. Squares are for DG structures, diamonds are for SG structures. The (100) DG mobility is lower that the SG mobility at high concentrations. Opposite behavior for (110) mobilities is observed.

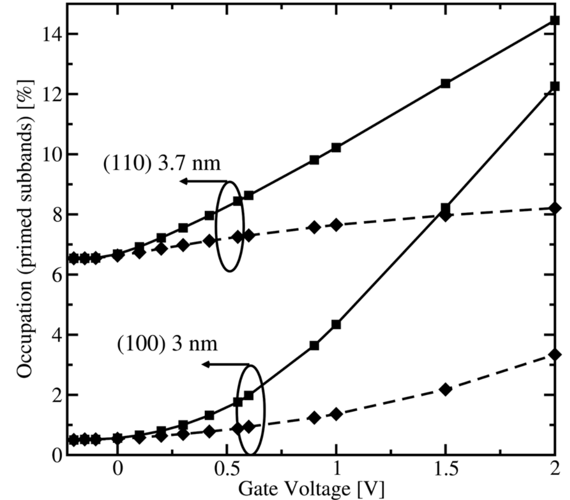

Fig. 2. Calculated relative occupation of primed subbands in (100) and (110) UTB FETs. Due to double carrier concentration for the same gate voltage, the primed ladder occupation (squares) is higher in both (100) and (110) orientation DG structures.

good agreement with the results obtained for an SG structure for both (100) and (110) orientations [20]. However, the mobility dependences are drastically different in ultrathin (100) and (110) structures.

For 3 nm body thickness the DG mobility, plotted as a function of $N_{\mathrm{DG}}/2$, tends to be slightly higher than the corresponding SG mobility at small N_{SG}. For high carrier concentrations the DG mobility for (100) orientation becomes lower than the SG mobility. This is in qualitative agreement with experimental data, also shown in Fig. 1. For (110) UTB FETs the DG mobility as a function of $N_{\mathrm{DG}}/2$ is higher than that for (110) SG structures, in the whole range of carrier concentrations N_{SG}. This is in agreement with recent experimental results [6] and is consistent with the concept of the mobility enhancement in DG UTB FETs due to volume inversion [5].

We note that the mobility plotted as a function of the total carrier concentration N_{DG} is always higher in DG structures [21]. We also note that in order to obtain a better quantitative agreement with the experimental mobility data, additional mechanisms such as interaction with surface optical phonons, scattering on fluctuations of δt_{SI} [7], [22], and scattering with interfacial and remote charges in the poly-gates [17], [23] could be included. Confinement of acoustic phonon modes relevant to UTB FET structures also improves agreement with the experimental data [24]. Our transport model, however, is sufficient to capture the main peculiarity of the mobility behavior in DG and SG structures at high concentrations.

The mobility in DG (100) UTB structures at high carrier concentrations is found to be lower than the mobility in SG FETs, from both the experiment and simulations. This is in contrast with the behavior expected from the volume inversion concept [5]. The difference in the mobility behavior in (100) and (110) DG structures was attributed to a higher occupation of primed subbands in (100) DG FETs compared to (110) FETs [6]. The higher primed subbands occupation was attributed to the difference in energy splitting between two- and fourfold degenerate subband ladders in SG and DG structures [6]. It was argued [6] that in (100) DG SOI FETs the intersubband energy splitting is smaller than in (100) SG structures, whereas in (110) SG and DG structures the splitting remains similar.

Although the energy splitting between primed and unprimed subbands is indeed smaller in DG structures, this mechanism cannot solely be responsible for a significant increase of the occupancy of primed subbands [20]. The physical reason is quite obvious: in UTB FETs the subband structure is mainly determined by the strong geometrical confinement of electrons within the thin body. Therefore, the subband structure in UTB DG and SG FETs is quite similar, even at high concentrations. The occupation of primed subbands in DG structures is significantly higher due to the following mechanism [20]. Since the SG and DG mobilities are compared as functions of concentration per *single* inversion layer, the DG FET contains almost twice as many carriers as the SG FET. This pushes the Fermi-level up and leads to significantly higher subband population in a DG UTB FET [20].

IV. Biaxial Strain

Double carrier concentration in DG structures leads to higher primed subband occupation in (110) DG FETs as well, as illustrated in Fig. 2. If the assumption adopted in [6] that a higher occupation of primed subbands results in the mobility lowering were correct, the DG mobility in (110) FETs should also rapidly decrease beyond its SG value at high concentrations. However, this contradicts experimental data and the results of simulations.

To study the influence of occupation of primed subbands on the mobility lowering in (100) DG FETs we apply a biaxial stress of 1.6 GPa. This level of stress is enough to provide an additional splitting between the primed and unprimed subbands to depopulate the primed ladder completely. Results of the mobility simulation in 3 nm DG and SG structures, with biaxial stress applied, are shown in Fig. 3 together with the results for the unstrained structure. Both mobilities in strained and unstrained structures are similar in the whole range of concentrations. The inset displays the population of primed subbands in a

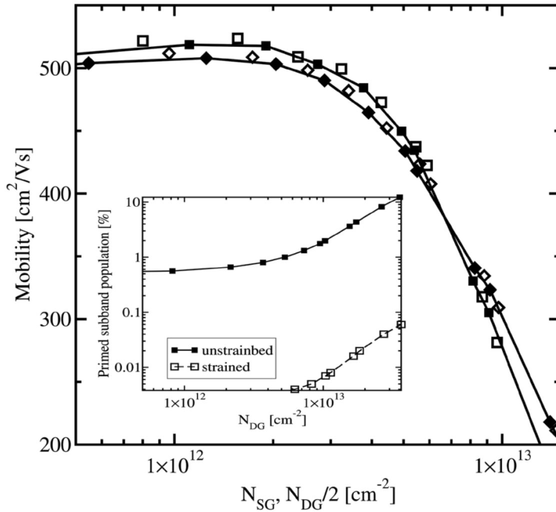

Fig. 3. Mobility in (100) 3 nm thick DG (squares) and SG (diamonds) structures computed with (open symbols) and without (closed symbols) in-plane biaxial stress of 1.6 GPa. Inset: occupation of primed subbands in relaxed (closed symbols) and biaxially stressed (open symbols) DG structure.

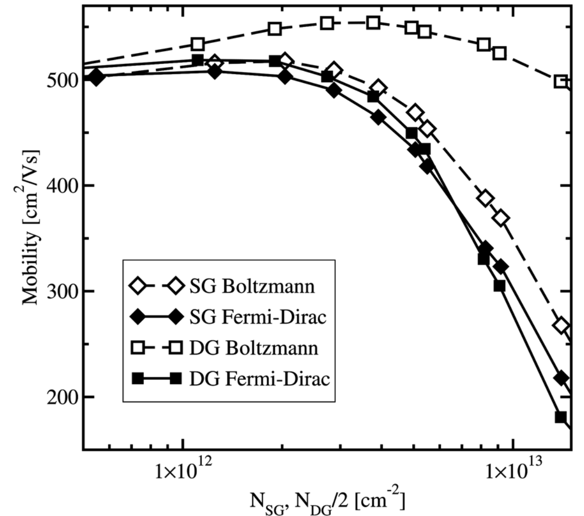

Fig. 5. Mobility in 3 nm (100) SG (diamonds) and DG (squares) structures computed with Boltzmann (open symbols) and Fermi–Dirac (closed symbols) statistics.

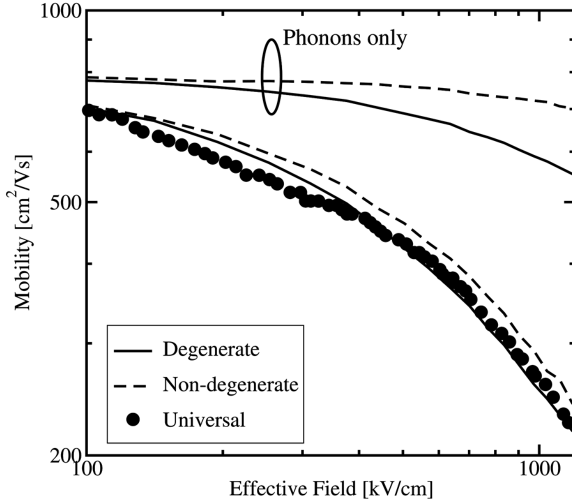

Fig. 4. Effective mobility of an Si inversion layer at (100) interface computed with Boltzmann (dotted line) and Fermi–Dirac (solid lines) statistics reproduces well the universal mobility curve [25] (circles). Phonon-limited mobility in degenerate and nondegenerate case is also shown.

3 nm DG structure. These results confirm that the primed ladder in a strained FET is completely depopulated. Since the mobilities of strained and unstrained UTB FETs are practically equivalent for both SG and DG structures, it then follows that the higher occupation of primed subbands is not the reason for the DG mobility lowering in (100) DG UTB structures.

V. Importance of Degeneracy Effects

Degeneracy effects in the scattering rates (2) may have an important influence on the mobility, especially at high inversion concentrations, and they require a special investigation. The phonon-limited mobility in inversion layers shows a different behavior if the Pauli exclusion principle is taken into account or not [26]. However, if surface roughness scattering is included, the universal mobility curve can be reproduced equally well using both degenerate and nondegenerate statistics, as shown in Fig. 4.

We note that the inversion layer subband structure calculated with the Fermi–Dirac distribution function for the carrier concentration is slightly different from that computed with the Boltzmann distribution function. However, for the practical range of effective fields considered here this difference was found to be small and does not affect the conclusion that the universal mobility curve is reproduced well independent on statistics.

In UTB FETs degeneracy effects are more pronounced, and their inclusion is crucial for accurate transport calculations. We consider an example a 3 nm (100) UTB FET. The nondegenerate statistics is assured by using the rates $S_{\rm mn}(\mathbf{k}',\mathbf{k})$ of the original Boltzmann equation in the Monte Carlo algorithm described above. Results of mobility calculations for SG and DG structures, with and without degeneracy effects taken into account in the Monte Carlo simulations are summarized in Fig. 5.

The difference between the mobility values for degenerate and nondegenerate statistics shown in Fig. 5 looks surprising. Indeed, at high carrier concentrations the principal scattering mechanism limiting the low-field mobility is elastic surface roughness scattering. For elastic scattering the forward and backward scattering rates are equal $S^{\rm el}_{\rm mn}(\mathbf{k}',\mathbf{k}) = S^{\rm el}_{\rm nm}(\mathbf{k},\mathbf{k}')$, so that the Pauli blocking factor cancels out from the equations for the elastic scattering rates (2), and degeneracy effects seem to be irrelevant. It is not correct, however, since the Pauli blocking factor is also present in the inelastic electron–phonon part of the total scattering integral and affects energy relaxation. The Pauli blocking factor in the electron–phonon scattering integral ensures the equilibrium solution to be the Fermi–Dirac distribution function.

In the degenerate case the Fermi level is pushed up leading to an increase of the average carrier energy for high N. This results in higher momentum transfer q due to scattering. Because the correlation function $S_{SR}(q)$ of the surface roughness (5) decreases with q, the mobility should increase. From this perspective it would be unclear why the degenerate electron mobility is substantially lower than the mobility in a nondegenerate case.

To resolve the apparent contradiction, we study the influence of static screening described by the dielectric function (6). Fig. 6

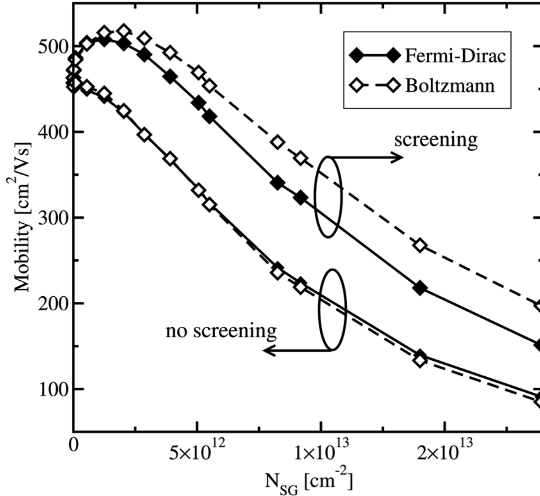

Fig. 6. Mobility of a 3 nm (100) SG FET computed with Boltzmann (open diamonds) and Fermi–Dirac (closed diamonds) statistics, with and without screening.

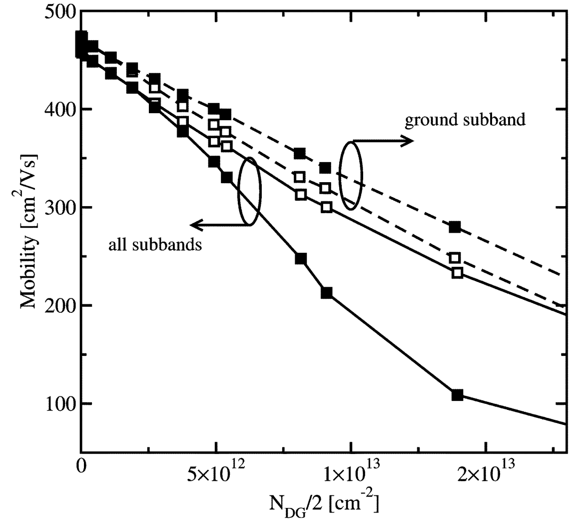

Fig. 7. 3 nm (100) DG FET mobilities computed for $\varepsilon(q) = 1$ with Boltzmann (open squares) and Fermi–Dirac (closed squares) statistics. Mobilities when only the ground subband is included in trasport calculations are also shown.

compares the mobilities in a 3 nm (100) SG FET calculated with and without screening effects. The dielectric function (6) of a quasi 2-D electron gas can be written in the form

$$\varepsilon(q) = 1 + \frac{q_0(q)}{q}$$

where q_0 is the inverse screening radius. Because $\varepsilon(q) \geq 1$ the mobility with screening included is higher than the mobility without screening in both degenerate and nondegenerate cases.

When screening is neglected, the SG mobilities computed with degenerate and nondegenerate statistics do (accidentally) coincide. With screening included, the nondegenerate SG mobility becomes higher than the degenerate mobility. This happens because the dielectric screening makes surface roughness components with q smaller than q_0 ineffective, reducing scattering of carriers with low energies. Since for fixed concentration the population of low-energy states is higher in the case of Boltzmann statistics, the screening is responsible, at least partly, for the relative mobility increase in the nondegenerate case.

Results of mobility calculations for a 3 nm (100) DG FET without screening are shown in Fig. 7. Even in this artificial case the nondegenerate mobility persists to be higher at high N_{DG} than the degenerate mobility. Therefore, screening can only be partly responsible for the mobility increase in the nondegenerate case, and the previously mentioned controversy still exists.

In DG structures the Fermi level is pushed higher and degeneracy is stronger than in SG structures due to double carrier concentration and degenerate statistics. This results in a substantial increase of relative occupation of higher subbands. Since the higher population of the primed subbands does not have a sensible influence on the mobility at high concentration, as it was shown by applying the biaxial stress, the reason should be the occupation of the higher unprimed subbands. In order to clarify the effect of occupation of higher unprimed subbands, we exclude the higher subbands from consideration by restricting the DG structure to an artificial "quantum limit". In this limit only the ground subband is used for transport simulations. Results of simulations in this limit are also shown in Fig. 7.

The nondegenerate mobility is not affected by the restriction to the ground subband and closely follows the nondegenerate mobility shown in Fig. 7. The degenerate mobility in the DG structure with only ground subband included is higher than the mobility for the nondegenerate case. The result of the Monte Carlo calculations are consistent with the analysis of scattering rates (2). Indeed, for the Gaussian correlation function (5) with screening neglected, the rate to scatter out from a state with energy E within the ground subband with the subband energy E_0 due to surface roughness can be computed as

$$\Gamma_{00}(E) = \frac{\hbar\pi\Delta^2\Lambda^2 m^*}{4m_z^2}\left[\psi_0'^4(0) + \psi_0'^4(t_{SI})\right] \times \exp(-y) I_0(y) \quad (7)$$

where $y = (E - E_0)m^*\Lambda^2/\hbar^2$, m^* is the effective mass, and $I_0(y)$ is the modified Bessel function. In the degenerate case the characteristic scattering rate determining is $\Gamma_{00}(E_F)$, whereas for the Boltzmann statistics it is $\Gamma_{00}(E_0)$ at the bottom of the ground subband. Since $\exp(-y)I_0(y)$ is a decreasing function, $\Gamma(E_F) < \Gamma(E_0)$ for $E_F > E_0$, and the degenerate mobility should be greater than the nondegenerate mobility in the structure with only a single subband, in agreement with our simulations in Fig. 7.

At high carrier concentrations, when E_F is becoming higher than the bottom E_1 of the next unprimed subband, elastic intersubband scattering will occur. Because of this additional scattering channel and a step-like increase of the density of after-scattering states, the scattering rate is sharply increased. The total scattering rate Γ_0 from a state in the ground subband with energy E is the sum with respect to the open channels n:

$$\Gamma_0(E) = \sum_n \Gamma_{0n}(E)$$

where

$$\Gamma_{0n}(E) = \Theta(E - E_n)\frac{\hbar\pi\Delta^2\Lambda^2 m^*}{4m_z^2} I_0(\xi) \times \left[\psi_0'^2(0)\psi_n'^2(0) + \psi_0'^2(t_{SI})\psi_n'^2(t_{\mathrm{SI}})\right] \times \exp\left(-\frac{(2E - E_0 - E_n)m^*\Lambda^2}{2\hbar^2}\right) \quad (8)$$

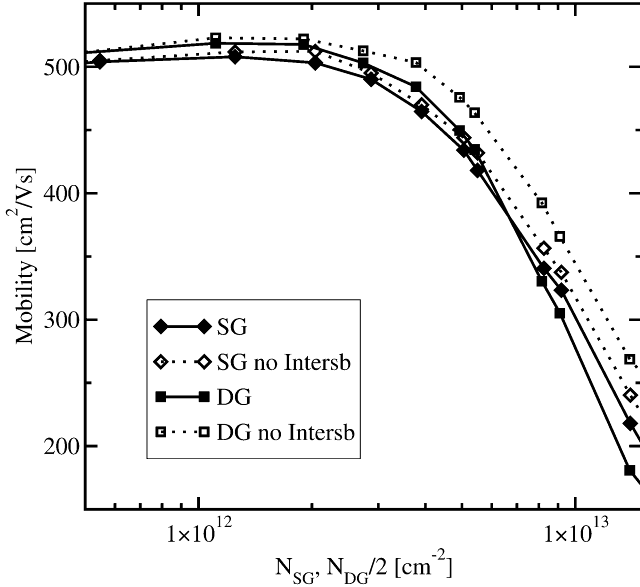

Fig. 8. Mobility in 3 nm thick (100) structures, computed with (solid lines) and without (dotted lines) intersubband scattering. Higher carrier concentration in a UTB DG structure (squares) at the same gate voltage pushes the Fermi-level up and opens additional intersubband scattering channels between unprimed subbands. It decreases the mobility in (100) UTB DG FETs below its SG values (diamonds) at high carrier concentrations.

where $\xi = m^* \sqrt{(E-E_0)(E-E_n)}\Lambda^2/\hbar^2$, and $\Theta(x)$ is the Heaviside function. The importance of intersubband scattering was predicted in [27] and recently studied experimentally [28]. To estimate the contribution of the intersubband scattering between the ground and the first unprimed subbands into $\Gamma_0(E)$, we set $E = E_1$. The ratio $\Gamma_{00}/\Gamma_{01} \propto \exp(\nu/2)/I_0(\nu)$ with $\nu = 0.5m^*(E_1 - E_0)\Lambda^2/\hbar^2$. For $\Lambda = 1.5$ nm and $t_{SI} = 3$ nm, $m^* = m_t = 0.19m_0$, and $m_z = m_l = 0.91m_0$, we have $\nu = 3.7$ and the ratio $\Gamma_{00}/\Gamma_{01} \approx 0.15$, such that the scattering rate is increases nearly by an order of magnitude. This effect smoothes out by integrating with the weight factor $f(E)(1-f(E))$ in the mobility expression [14].

To demonstrate the importance of intersubband scattering for the mobility calculations, we artificially switch off the scattering between the lowest and higher unprimed subbands. We consider degenerate statistics and restore screening. Results of the mobility calculations for a 3 nm UTB structure, with and without intersubband scattering are shown in Fig. 8. Without intersubband scattering, the DG FET mobility is higher than the corresponding SG mobility, in compliance with the volume inversion concept [5]. It confirms our finding that as soon as the additional intersubband scattering channel becomes activated, the DG mobility value sinks below the SG mobility.

Because the quantization mass $m_z = 2m_l m_t/(m_l + m_t)$ of unprimed subbands at (110) interface is nearly three times lower than m_l, the separation between unprimed subbands is significantly higher in (110) UTB FETs that in (100) UTB FETs. Because of the higher separation and due to higher density of states, only the ground subband from the ladder of fourfold degenerate unprimed subbands remains populated in (110) UTB structures. Contrary to (100) FETs, the higher unprimed subbands remain virtually depopulated in (110) UTB FETs. Therefore, the additional channel of intersubband scattering is not activated even at high carrier concentrations. Due to volume inversion, the (110) DG mobility remains higher than its SG counterpart in the whole range of N, in agreement with the experiment [6].

VI. Conclusion

The mobility in DG and SG UTB FETs for substrate orientation (100) and (110) is theoretically investigated. The method is based on the solution of the linearized Boltzmann equation by the Monte Carlo procedure and allows the exact treatment of the Pauli exclusion principle in the limit of vanishing driving fields. Our approach is valid for arbitrary scattering rates and includes realistic band structure. Our results are in good agreement with experimental data for (110) UTB FETs, confirming the mobility enhancement in DG operation mode over the SG operation mode due to volume inversion. By applying biaxial strain it is shown that within our model the higher occupation of primed subbands is not the reason for the (100) DG mobility lowering beyond its SG value at high effective fields and cannot explain an apparent contradiction with the volume inversion hypothesis. It is demonstrated that degeneracy effects play a significant role in compensating the volume inversion induced mobility enhancement in (100) DG structures. These effects lead to a significant occupation of higher subbands in the unprimed ladder as well as to an increased intersubband scattering, which decreases the mobility in the lowest subband of DG (100) FETs. Due to different quantization masses for (110) UTB orientation, these effects are absent in (110) UTB FETs.

References

[1] K. K. Likharev, "Sub-20-nm electron devices," in *Advanced Semiconductor and Organic Nano-Techniques*. New York: Academic, 2003, pp. 239–302.

[2] V. Sverdlov *et al.*, "Nanoscale silicon MOSFETs: A theoretical study," *IEEE Trans. Electron Devices*, vol. 50, no. 9, pp. 1926–1926, Sep. 2003.

[3] F. Gámiz *et al.*, "Electron mobility in double gate silicon on insulator transistors: Symmetric-gate versus asymmetric-gate configuration," *J. Appl. Phys.*, vol. 94, no. 9, pp. 5732–5732, 2003.

[4] D. E. Esseni *et al.*, "Physically based modeling of low field electron mobility in ultrathin single- and double-gate SOI n-MOSFETs," *IEEE Trans. Electron Devices*, vol. 50, no. 12, pp. 2445–2445, Dec. 2003.

[5] F. Balestra *et al.*, "Double-gate silicon-on-insulator transistor with volume inversion: A new device with greatly enhanced performance," *IEEE Electron Device Lett.*, vol. 8, no. 9, pp. 410–410, Sep. 1987.

[6] G. Tsutsui, "Mobility enhancement due to volume inversion in (110)-oriented ultrathin body double-gate nMOSFETs with body thickness less than 5 nm," in *IEDM Tech. Dig.*, 2005, pp. 747–750.

[7] K. Uchida *et al.*, "Experimental study on carrier transport mechanisms in double- and single-gate ultrathin-body MOSFETs—Coulomb scattering, volume inversion, and δT_{SOI}-induced scattering," in *IEDM Tech. Dig.*, 2003, pp. 805–808.

[8] S. Smirnov *et al.*, "Monte Carlo method for modeling of small signal response including the Pauli exclusion principle," *J. Appl. Phys.*, vol. 94, no. 9, pp. 5791–5791, 2003.

[9] L. Reggiani *et al.*, "Diffusion and fluctuations in a nonequilibrium electron gas with electron–electron collisions," *Phys. Rev. B*, vol. 40, no. 18, pp. 12 209–12 209, 1989.

[10] F. Stern and W. E. Howard, "Properties of semiconductor surface inversion layers in the electric quantum limit," *Phys. Rev.*, vol. 163, no. 3, pp. 816–835, 1967.

[11] P. J. Price, "Resonant tunneling via an accumulation layer," *Ann. Phys.*, vol. 133, pp. 217–217, 1981.

[12] C. Jacoboni and L. Reggiani, "The Monte Carlo method for the solution of charge transport in semiconductors with applications to covalent materials," *Rev. Mod. Phys.*, vol. 55, no. 3, pp. 645–645, 1983.

[13] R. E. Prange and T. W. Nee, “Quantum spectroscopy of the low-field oscillations in the surface impedance,” *Phys. Rev.*, vol. 168, no. 3, pp. 779–786, 1968.

[14] M. V. Fischetti *et al.*, “Six-band K.P calculation of the hole mobility in silicon inversion layers: Dependence on surface orientation, strain, and silicon thickness,” *J. Appl. Phys.*, vol. 94, no. 2, pp. 1079–1095, 2003.

[15] D. Esseni, “On the modeling of surface roughness limited mobility in SOI MOSFETs and its correlation to the transistor effective field,” *IEEE Trans. Electron Devices*, vol. 51, no. 3, pp. 394–394, Mar. 2004.

[16] C. Jungemann *et al.*, “Simulation of linear and nonlinear electron transport in homogenous silicon inversion layers,” *Solid-State Electron.*, vol. 36, no. 11, pp. 1529–1540, 1993.

[17] D. Esseni and A. Abramo, “Modeling of electron mobility degradation by remote coulomb scattering in ultrathin oxide MOSFETs,” *IEEE Trans. Electron Devices*, vol. 50, no. 7, pp. 1665–1674, Jul. 2003.

[18] D. K. Ferry and S. M. Goodnick, *Transport in Nanostructures*. Cambridge, U.K.: Cambridge Univ. Press, 1997.

[19] M. V. Fischetti and S. E. Laux, “Monte Carlo study of electron transport in silicon inversion layers,” *Phys. Rev. B*, vol. 48, no. 4, pp. 2244–2274, 1993.

[20] V. Sverdlov *et al.*, “Volume inversion mobility in SOI MOSFETs for different thin body orientations,” *Solid-State Electron.*, submitted for publication.

[21] D. Esseni *et al.*, “An experimental study of mobility enhancement in ultrathin SOI transistors operated in double-gate mode,” *IEEE Trans. Electron Devices*, vol. 50, no. 3, pp. 802–808, Mar. 2003.

[22] D. Esseni and A. Abramo, “Mobility modelling of SOI MOSFETs,” *Semicond. Sci. Technol.*, vol. 19, pp. S67–S70, 2004.

[23] F. Gámiz *et al.*, “Monte Carlo simulation of remote-coulomb-scattering-limited mobility in metal-oxide-semiconductor transistors,” *Appl. Phys. Lett.*, vol. 82, no. 19, pp. 3251–3253, 2003.

[24] L. Donetti *et al.*, “Influence of acoustic phonon confinement on electron mobility in ultrathin silicon on insulator layers,” *Appl. Phys. Lett.*, vol. 88, no. 1, pp. 122 108-1–122 108-3, 2006.

[25] S. I. Takagi *et al.*, “On the universality of inversion layer mobility in SI MOSFET’s: Part I—Effects of substrate impurity concentration,” *IEEE Trans. Electron Devices*, vol. 41, no. 12, pp. 2357–2362, Dec. 1994.

[26] E. Ungersboeck and H. Kosina, “The effect of degeneracy on electron transport in strained silicon inversion layer,” in *Proc. Int. Conf. Simulation of Semiconductor Processes and Devices*, 2005, pp. 311–314.

[27] L. Lucci *et al.*, “Comparative analysis of basic transport properties in the inversion layer of bulk and SOI MOSFETs: A Monte-Carlo study,” in *Proc. Int. Conf. Simulation of Semiconductor Processes and Devices*, 2004, pp. 321–324.

[28] K. Takashina *et al.*, “Intersubband scattering in double-gate MOSFETs,” *IEEE Trans. Nanotechnol.*, vol. 5, no. 5, pp. 430–430, Sep. 2006.

Viktor Sverdlov received the M.S. and Ph.D. degrees in physics from the State University of St. Petersburg, Russia, in 1985 and 1989, respectively.

From 1989 to 1999 he worked as a Staff Research Scientist at the V. A. Fock Institute of Physics, State University of St. Petersburg. In 1999 he became a Research Scientist at the State University of New York, Stony Brook. He joined the Institute for Microelectronics, Technische University Wien, Vienna, Austria, in 2004. His scientific interests include device simulations, computational physics, solid-state physics, and nanoelectronics.

Stephan Enzo Ungersback was born in Vienna, Austria, in 1977. He studied Physics at the Technische University Wien, Vienna, where he received the degree of Diplomingenieur in May 2002. He joined the Institute for Microelectronics in June 2002, where he is currently working on the Ph.D. degree.

He held a visiting research position at the Samsung Advanced Institute of Technology in Seoul, Korea, in summer 2003. His scientific interests include Monte Carlo simulation, band structure calculations, simulation of carbon nanotubes, and quantum mechanical confinement in submicrometer MOSFETs.

Hans Kosina (S’89–M’93) received the Diplomingenieur degree in electrical engineering and the Ph.D. degree from the Technische University Wien, Vienna, in 1987 and 1992, respectively.

He was for one year with the Institute of Flexible Automation at the Technische University Wien, and joined then the Institute for Microelectronics, where he is currently an associate professor. He received the venia docendi degree in microelectronics in 1998. In summer 1993 he was a Visiting Scientist at Motorola Inc., Austin, TX, and in summer 1999 a Visiting Faculty Member at Intel Corp., Santa Clara, CA. His current research interests include device modeling of semiconductor devices, nanoelectronic devices, organic semiconductors and optoelectronic devices, development of novel Monte Carlo algorithms for classical and quantum transport problems, and computer-aided engineering in ULSI-technology.

Dr. Kosina has served as a Technical Program Committee member in the IEEE International Workshop on Computational Electronics in 2003 and 2004 and has been chairman of the 11th International Workshop on Computational Electronics held in Vienna in May 2006. He has been Associate Editor of the IEEE TRANSACTIONS ON COMPUTER-AIDED DESIGN OF CIRCUITS AND SYSTEMS since January 2004.